Studies on ZnO Nanorods Synthesized by Hydrothermal Method and their Characterization

B.H. Soni*, M.P. Deshpande†, S.V. Bhatt, N. Garg, S.H. Chaki

Department of Physics, Sardar Patel University, Vallabh Vidyanagar-388 120, Gujarat, India

ZnO nanorods, with a wide band gap of 3.37 eV have been attracting much attention due to its wide range of applications. Looking to this aspect in the present paper, ZnO nanorods were synthesized by hydrothermal method at 120 °C for 2 hrs in an autoclave by using zinc acetate and sodium hydroxide as the starting materials. The final product obtained was then characterized by Energy Dispersive analysis of X-rays (EDAX), X-ray powder diffraction (XRD), transmission electron microscopy (TEM), selected area electron diffraction (SAED) and Raman Spectroscopy. X-ray diffraction and Raman spectra showed that ZnO nanorods are belonging to wurtzite structure without any impurity phases. The ZnO nanorods shows polycrystalline behaviour as observed from SAED pattern and the calculated lattice parameters from this pattern which matches with the XRD results. The optical properties of the ZnO nanorods were then further studied with the help of absorption, photoluminescence (PL) and FTIR spectra. The optical energy band gap determined from the absorption spectra comes about 3.33 eV. In the photoluminescence spectra of ZnO nanorods the UV emission appears at 380 nm and strong blue emission appears at 445 nm. FTIR spectra indicate the existence of distinct characteristic absorption peak at 520 cm^{-1} for ZnO stretching modes. The potential toxicity of nanosized ZnO nanorods were investigated using Staphylococcus aureus, Escherichia coli, Bacillus subtilis, Pseudomonas aeruginosa, Serratia marceseus and Proteus vulgaris bacteria as test organism.

Keywords: ZnO nanorods, Hydrothermal method, Raman spectra, Photoluminescence, Antibacterial.

PACS numbers: 61.46.Km, 87.85.Rs

1. INTRODUCTION

It is well known that both the shape and size of inorganic materials have a strong influence on electrical and optical properties. In recent years, the research area of one-dimensional (1D) semiconductor nanostructures is attracted much attention due to their unique properties and wide potential in nanodevices. Extensive efforts have been focused on many different morphological zinc oxide nanostructures, including nanowires [1], nanorods [2], nanocables [3] and nanobelts [4] and in correlating their morphologies with their size-related optical and electrical properties. In the past few years, much effort has been devoted to developing various 1D semiconductor nanostructures [5, 6]. Vapour-liquid- solid (VLS) [7] and vapour-solid (VS) [8] mechanisms for growth of whiskers or fibres at high temperature are well recognized, and have been used to synthesize various group III-V and II-VI compound semiconductor nanostructures [9, 10]. 1D semiconductor nanostructures have also been obtained via laser ablation-catalytic growth [11], oxide-assisted growth [12], template-induced growth [13], solution-liquid-solid growth in organic solvents [14] and metal-organic chemical vapour deposition (MOCVD) [15]. In this work, ZnO nanorods are synthesized by hydrothermal technique. Hydrothermal technique is a promising alternative synthetic method because of the low process temperature and very easy to control the particle size. The hydrothermal process have several advantage over other growth processes such as use of simple equipment, catalyst-free growth, low cost, large area uniform production, environmental friendliness and less hazardous [16].

Zinc oxide (ZnO) is a wide and direct band gap (3.37 eV) semiconductor with a large exciton binding energy (60 meV) exhibiting near UV emission, transparent conductivity and piezoelectricity [17]. It has various applications in blue and ultraviolet optical devices such as light-emitting diodes, UV detectors [18], field emission [19, 20], high sensitivity gas sensors [21, 22], biosensors [23], dye-sensitized solar cells [24], photoluminescent materials [25], photocatalytic degradation of pollutants [26, 27] and antibacterial treatment [28, 29] and laser diodes [30]. Furthermore, ZnO is bio-safe and biocompatible, and may be used for biomedical applications without coating. ZnO demonstrates significant growth inhibition of a broad spectrum of bacteria [31, 32]. The suggested mechanism for the antibacterial activity of ZnO is based mainly on catalysis of formation of reactive oxygen species (ROS) from water and oxygen [33-37] that disrupt the integrity of the bacterial membrane, although additional mechanisms are also been suggested [38-44].

2. EXPERIMENTAL DETAILS

In a typical experiment, all the reagents were analytically pure and used without further purification. To synthesize ZnO nanorods, a stock solution of 0.1 M Zinc acetate dihydrate was prepared in 50 ml methanol under stirring. To this stock solution 15 ml of 0.5M Sodium Hydroxide solution prepared in methanol was added under continuous stirring for 30 min in order to get the pH value of the reactants 10.6. This solution was transferred into steel lined sealed stainless steel autoclave and maintained at temperature 120 °C for 2 hrs under autogenous pressure. Then, it was allowed to cool naturally to room temperature. After the reaction was completed, the resulting white solid products were

---

* bindiyasoni80@yahoo.com

† vishwadeshpande@yahoo.co.in

washed with methanol several times to remove impurities, filtered and then dried in an oven at 60 °C for 24 hrs. The chemical process leading to ZnO formation of considered according to the following:

$$Zn(CH_3COO)_2 + NaOH \rightarrow$$
$$Zn(CH_3COO)OH + Na(CH_3COO) \qquad (2.1)$$

$$Zn(CH_3COO)OH + NaOH \rightarrow ZnO +$$
$$Na(CH_3COO) + H_2O \qquad (2.2)$$

Energy dispersive analysis of X-rays (EDAX) attached to Philips EM 400 electron microscope is used for determining composition of ZnO nanorods. The XRD pattern was taken on a Philips Xpert MPD, X-ray diffractometer with CuKα radiation ($\lambda = 1.54$ Å). The scan rate of 0.20°/s was used to record the pattern in the range of 3°-99.97°. Transmission electron microscopy (TEM) patterns taken were used to study the size, shape and surface morphology of the synthesized nanorods. The Raman experiments was done at room temperature under the backscattering geometry using a Jobin-Yvon Horiba LabRam, HR800 single monochromator coupled with "Peltier cooled" charged coupled device (CCD) with the help of 488 nm Argon (Ar+) laser as excitation source. The optical absorption spectra was taken with the help of a Perkin Elmer Lambda-19 UV-Vis-NIR spectrophotometer. Photoluminescence (PL) spectra was obtained by FluoroMax-Compact Spectrofluorometer with a Xe lamp at room temperature. Fourier transform infrared spectroscopy (FTIR) absorption was measured for KBr supported samples over the frequency range of 4000-400 cm^{-1} and at a resolution of 0.15 cm^{-1}, using a model Perkin Elmer Spectrum GX.

3. RESULTS AND DICUSION

3.1 Energy Dispersive Analysis of X-rays (EDAX)

Fig. 1 shows the EDAX spectra of ZnO sample which clearly reflect the absentia of other impurities and contaminants in the samples. According to quantitative analysis of EDAX, the weight percentage ratio of Zinc (Zn) to Oxygen (O) comes out to be 79.50 : 20.50, which is almost consistent with stoichiometric ZnO.
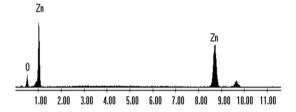

Fig. 1 – EDAX Spectra of ZnO sample

3.2 X-ray Diffraction Studies

XRD pattern shown in Fig. 2 of as prepared ZnO sample indicates the presence of the sixteen prominent peaks which are indexed based on hexagonal wurtzite structure. The lattice parameters 'a' and 'c' of this hexagonal phase are 3.25 Å and 5.20 Å, respectively ($c/a = 1.60$) are calculated from the powderX software

giving a good resemblance with standard JCPDS (Joint Committee for Powder Diffraction Standard) file No.1314-13-2.
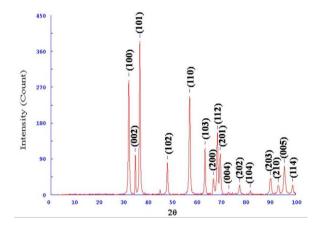

Fig. 2 – X-ray diffractogram of ZnO sample

To calculate crystallite size and strain broadening we used Hall Williamson relation [45] given as

$$\beta\cos\theta/\lambda = K/D + 4\varepsilon\sin\theta/\lambda \qquad (3.3)$$

where λ represent the wavelength of the X-ray radiation CuKα ($\lambda = 1.54$ Å), β is the full width at half maximum of the diffraction peak (in radian), θ is Bragg's angle, K is constant quantity taken as unity by assuming the crystallites to be spherical in shape and ε is strain broadening.
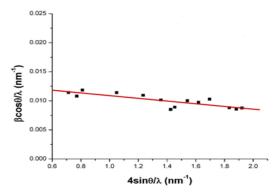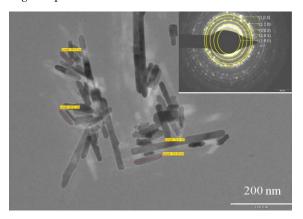

Fig. 3 – Hall Williamson plot for ZnO sample

Fig. 3 shows the plot of $\beta\cos\theta/\lambda$ versus $4\sin\theta/\lambda$ for ZnO sample giving a straight line with slope ε and intercept K/D. The average crystallite size (D) obtained from Hall-Williamson plot was found to be 7.5 nm. The slope of the Hall-Williamson plot gives the amount of residual strain, which turns out to be -2.32×10^{-3} and the negative value of residual strain indicates that compressive strain is dominating.

3.3 Transmission Electron Microscopy (TEM)

TEM was employed to further investigate the structural details of the ZnO sample. Typical TEM image and selected area electron diffraction pattern obtained from the ZnO nanorods are shown in Fig. 4. A statistical analysis reveals that the average nanorods diameters and lengths range from 25 to 30 nm and ~ 0.3 to 3 μm, respectively. The selected area electron

diffraction pattern (SAED) indicates (inset) that the synthesized nanorods are polycrystalline in nature. The diffracting planes are indexed as (103), (110), (102), (101) and (100) reflections which are corresponding to the hexagonal phase of ZnO.

Fig. 4 – TEM image and selected area electron diffraction pattern of ZnO nanorods

After recording the diffraction pattern, we used the following equation (3.4) derived from the Bragg equation to calculate the 'd' spacing.

$$d_{hkl} = \lambda L / R \qquad (3.4)$$

where, R is the distance from the central bright spot to corresponding rings, L is the camera length between specimen and photographic film and λ is the wavelength of the electron beam based on the accelerating voltage: 200 Kv = 0.02736 Å. The lattice parameters were estimated from the equation:

$$\frac{1}{d_{hkl}^2} = \frac{4}{3\left[a^2\left(h^2 + hk + k^2\right) \right]} + \frac{l^2}{c^2} \qquad (3.5)$$

where a and c are the lattice parameters and h, k and l are the Miller indices and d_{hkl} is the interplanar spacing for the plane (hkl). The lattice parameters 'a' and 'c' calculated from TEM using equation (3.5) are found to be 3.23 Å and 5.18 Å respectively which is consistent with the above XRD results.

3.4 Raman spectra studies

In nanocrystalline materials, $q \approx 0$ selection rule is relaxed due to interruption of lattice periodicity. In bulk crystals, the phonon eigen state is a plane wave and the selection rule for Raman scattering is $q \approx 0$, where q is the wave vector. But in nanocrystallites, the spatial correlation function of the phonons is finite due to the phonon confinement, and hence $q \approx 0$ selection rules is relaxed and Raman signals from the phonon branch away from the zone centre also contribute to the resultant Raman line. A primitive ZnO cell has four atoms (two formula units), each of which occupies C_{3v} sites, leading to 12 phonon branches (nine optical and three acoustic). ZnO has phonon dispersion relations consisting of 12 branches whose group-theoretical analysis at Brillouin center ($q = 0$) yields decomposition into the following phonon modes:

$$\Gamma = 2 \times \left(A_1 + B_1 + E_1 + E_2\right) \qquad (3.6)$$

Among these modes, there are acoustic modes with $\Gamma_{acous} = A_1 + E_1$ and optical modes with $\Gamma_{opt} = A_1 + (2 \times B_1) + E_1 + (2 \times E_2)$. Of these the B_1 modes are silent modes and other modes are Raman active [46, 47]. The Raman spectra of ZnO nanorods in the range 280-850 cm^{-1} fitted with the Lorentzian function are shown in Fig. 5.
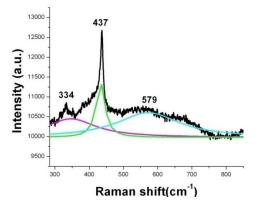

Fig. 5 – The Raman spectra of ZnO nanorods

The peak at 437 cm^{-1} is attributed to ZnO non-polar optical phonons E_2 mode, which is typical of one of Raman active branches. The peak at 334 cm^{-1} attributed to $E_2^{high} - E_2^{low}$ mode. The origination of a very short peak at 579 cm^{-1} attributed as E_1^{low} was also observed. The appearance of E_1^{low} mode is supposed to be because of the structural defects (oxygen vacancies, zinc interstitial and free carriers) and impurities. The higher intensity and narrower spectral width of the Raman active E_2 mode indicated that the as-grown ZnO nanorods have good quality with a hexagonal wurtzite crystal phase.

3.5 UV-Vis-NIR Spectroscopy

The UV absorbance spectra of ZnO nanorods dispersed in methanol is shown in the Fig. 6. The spectrum shows an absorption edge at 372 nm that is blue shifted with respect to the bulk absorption edge which appears at 376 nm, this shift may be ascribed to the nano size effect of the synthesized ZnO. There is a blue-shift in the band-edge with diminishing diameter of the nanorods. The lower diameter of nanorods provides a higher quantum confinement exciton effect, the reason being the electron and holes are confined in the very small area that makes them coupled together further and move only in a potential well. For the ZnO nanorods with diameters 25-30 nm synthesized here, the quantum confinement effect may not be strong enough. Therefore, the blue-shift shown in this figure 6 can possibly be attributed to the higher defect density on surface of nanorods with lower diameters which may be expected to provide new bound excitons with new binding energies which can result in spectral shift in nanostructures with different sizes due to greater surface-to-volume ratio.

The band gap of ZnO nanorods is determined by using the expression $\alpha h\upsilon = C (h\upsilon - E_g)^n$ where $h\upsilon$ is the photon energy, E_g is the optical energy band gap, C is a
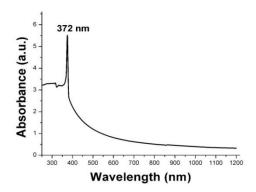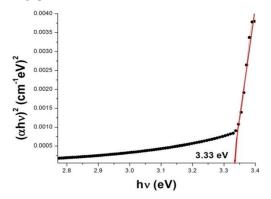
Fig. 6 – Absorption spectra of ZnO nanorods

constant and *n* is an index whose value is taken depending on the type of transition responsible for the absorption. For direct transition $n = ½$ was found to be more suitable for ZnO. In Fig. 7 the relation between $(\alpha h\nu)^2$ and $h\nu$ is plotted and the value of the optical band gap obtained comes out to be 3.33 eV.

Fig. 7 – Plot of $(\alpha h\nu)^2$ vs $h\nu$ for ZnO nanorods

3.6 Photoluminescence Spectroscopy

Photoluminescence measurements were carried out at room temperature using xenon lamp as source at different excitation wavelength of 325 nm, 330 nm and 370 nm. The PL spectrum fitted with the Lorentzian function shows peaks at 380 nm (3.27 eV), 445 nm (2.79 eV) and 520 nm (2.39 eV) is shown in Fig. 8.

It was reported that the visible emissions are related to several intrinsic defects in ZnO materials, which include Zn vacancies (V_{Zn}), O vacancies (V_O), interstitial Zn (Zn_i), interstitial O (O_i), and substitution of O at Zn position (O_{Zn}) [48-50]. Xu et al. [51] had calculated the energy levels of the intrinsic defects in ZnO using the full-potential linear muffin-tin orbital (FP-LMTO) method and the values can be seen in Table 1.

Thus, if we look at Fig. 8 then we could observe the UV emission peak at 380 nm which can be attributed to the exciton emission from conduction band to valence band. The blue emission which is at 445 nm probably caused by two defects' levels, either transition from Zn_i to valence band (VB) (2.9 eV) or transition from the bottom of the conduction band (CB) to O_i level (2.98 eV), according to the calculated results of Xu et al [51]. The electronic transition for blue emission most likely occurs from the donor level of Zn interstitial to acceptor energy level of Zn vacancy. The visible luminescence of ZnO mainly originates from different
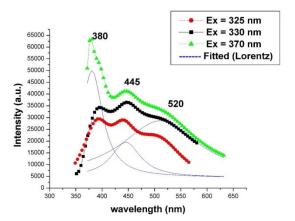

Fig. 8 – PL spectra of ZnO nanorods

Table 1 – Calculated emission energies of various transitions originating from the intrinsic point defect levels in ZnO [51]

Energy interval	Position in the energy gap	Value of energy (eV)
CB-VB	From conduction band to valence band (energy gap)	3.37
CB-V_{Zn}	From conduction band to V_{Zn}	3.07
CB-V_O	From conduction band to V_O	1.82
Zn_i-VB	From Zn_i to valence band	2.90
Zn_i-V_{Zn}	From Zn_i to V_{Zn}	2.70
Zn_i-O_i	From Zn_i to O_i	2.50
CB-O_i	From conduction band to O_i	2.98
CB-O_{Zn}	From conduction band to O_{Zn}	2.37

defect states such as oxygen vacancies and Zn interstitials. The green emission peak (520 nm) which has the lowest intensity of emission in the spectra, almost coincided with the energy interval from the bottom of the conduction band to the O_{Zn} level (2.36 eV), according to table 1. The peak around 520 nm is a green emission assigned to singly ionised oxygen vacancy. Green emission is attributed due to the recombination of photogenerated holes with the electrons belonging to oxygen vacancy states on the surface [52-55]. It can be seen from these results that emission properties are strongly dependent on defects that are presented in the ZnO nanorods.

3.7 FTIR Spectroscopy

The FTIR spectra taken at room temperature in the range of 400-4000 cm^{-1} is shown in Fig. 9. The obtained spectrum shows an absorption band around 520 cm^{-1}, which is the typical characteristic band of the wurtzite hexagonal phase pure ZnO. The two strong peaks at 1553 cm^{-1} and 1394 cm^{-1} that may be assigned to the symmetric starching of carboxylate group (COO$^-$) probably from the small residue of zinc acetate used in reaction. The broad absorption peak around 3479 cm^{-1} is due to O-H stretching and peak around 2933 cm^{-1} is due to C-H (acetate) stretching [55].
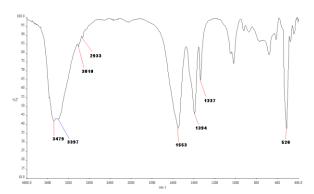
Fig. 9 – FTIR reflection spectra of the ZnO nanorods

3.8 Bacterial cultures and evaluation of anti-bacterial activities

Master solution

To make dispersed ZnO nanorods for the antibacterial test, we took a preset amount of dry ZnO nanorods mixed with distilled water in a glass beaker separately with the aid of stirrer. Once the nanorods were dispersed in water the beaker was placed in an ultrasonicator. The reason for the use of sonication was to break down the agglomerate. After 30 min of sonication the so called dispersed ZnO nanorods were produced which had concentration of 5 mg/ml. Similar procedure was followed to obtain disperse ZnO nanorods in methanol medium.

Culture and Inoculums

Standard bacterial cultures *Staphylococcus aureus*, *Escherichia coli*, *Bacillus subtilis*, *Pseudomonas aeruginosa*, *Serratia marceseus*, *Proteus vulgaris* were procured as from B. R. D school of Biosciences, S. P. University, Gujarat. The bacterial cultures were streaked to check the purity and a single colony was inoculated in 5 ml Luria Bertani broth, incubated overnight at 30 °C, 150 rpm. We determined the optical densities of the actively growing cultures by measuring absorbance at 600 nm.

Agar diffusion method

The anti-bacterial / microbial activity was studied using gel diffusion method [56]. 100 µl of actively growing target culture was affixed with 5 ml of 1 % top agar vortexed and pour onto the agar plate, allowed to solidify. The solidified plate was bored to form 5 wells of 4 mm diameter using cork borer. The wells were then inoculated with 100 µl aliquots of 5 mg/ml dispersed ZnO nanorods. The nanorods were allowed to diffuse into the agar followed by incubating the plates at 30 °C for 48 hours. Upon incubation the zone of clearance around the wells were measured and evaluated with respect to water / methanol media respectively. The results of the quantitative antibacterial assessment by agar diffusion are shown in Table 2.

No antibacterial activity was found against the Escherichia coli for the samples dispersed in water medium. The Bacillus subtilis exhibits the strongest antibacterial activity in both media compared to the other test microorganisms. The reason for the difference

Table 2 – Antibacterial assessment by agar diffusion method

Test Organisms	ZnO nanorods dispersed in water medium	ZnO nanorods dispersed in methanol medium
Diameter of the clear inhibition zone (mm)		
S. aureus	6	3
Escherichia coli	-Nil-	8
Bacillus subtilis	8	13.5
P. aeruginosa	3.5	2.5
S. marceseus	5	1
Proteus vulgaris	1	5

in the antibacterial activity for different test microorganisms may be due to the difference in structure and thickness of the membrane cell wall. The presence of an inhibition zone clearly indicates that the mechanism of the biocidal action of ZnO involves disrupting the membrane. The mechanisms of the antibacterial activity of ZnO particles are not well understood although [57, 58] proposed that the generation of hydrogen peroxide be a main factor of the antibacterial activity, while [59] indicated that the binding of the particles on the bacteria surface due to the electrostatic forces could be a mechanism. However, a few studies have suggested that the primary cause of the antibacterial function might be from the disruption of cell membrane activity [60]. Another possibility could be the induction of intercellular reactive oxygen species, including hydrogen peroxide (H_2O_2), a strong oxidizing agent harmful to bacterial cells [61, 62]. It has also been reported that ZnO can be activated by UV and visible light to generate highly reactive oxygen species such as OH^-, H_2O_2, and O_2^{2-}.

4. CONCLUSIONS

Using hydrothermal technique, we successfully synthesized ZnO nanorods having average diameter 25-30 nm. The XRD and SAED patterns clearly showed the formation of a single-phase compound with wurtzite structure having lattice parameter $a = 3.25$ Å and $c = 5.20$ Å. Photoluminescence analysis shows that many defects such as interstitial zinc, zinc vacancy and oxygen vacancy are responsible for this property. ZnO nanorods have a very strong photoluminescence band at visible range accompanied by few weaker defect states emissions which agrees well with the measurements from Raman spectroscopy. The optical absorption properties of this material may be very interesting for further application on catalyst and chemical sensors. Furthermore, the FTIR trace showed a broad absorption band related to Zn-O bond vibration. From the antibacterial study it is observed that ZnO nanorods were found to have strong antibacterial potential against *Bacillus subtilis* and weak antibacterial potential against *Escherichia coli*.

REFERENCES

1. Z.W. Pan, S. Dai, C.M. Rouleau, D.H. Lowndes, *Angew. Chem. Int. Ed.* **44** No 2, 274 (2005).
2. X.D. Wang, C.J. Summers, Z.L. Wang, *Nano Lett.* **4**, 423 (2004).
3. Y. Zhang, K. Suenaga, C. Collies, S. Lijima, *Science* **281**, 973 (1998).
4. Z.W. Pan, Z.R. Dai, Z.L. Wang, *Science* **291**, 1947 (2001).
5. A.M. Morales, C.M. Lieber, *Science* **279**, 208 (1998).
6. X.G. Peng, J. Wickham, A.P. Alivisatos, *J. Am. Chem. Soc.* **120** No 21, 5343 (1998).
7. A.I. Klimovskaya, I.P. Ostrovskii, A.S. Ostrovskaya, *phys. status solidi a* **153**, 465 (1996).
8. Y. Iwao, S.J. Hajime, *J. Cryst. Growth* **45**, 511 (1978).
9. T.J. Trentler, K.M. Hickman, S.C. Goel, A.M. Viano, P.C. Gibbons, W.E. Buhro, *Science* **270**, 1791 (1995).
10. J.Q. Hu, Q. Li, N.B. Wong, C.S. Lee, S.T. Lee, *Chem. Mater.* **14**, 1216 (2002).
11. X.F. Duan, C.M. Lieber, *J. Am. Chem. Soc.* **122**, 188 (2000).
12. R.Q. Zhang, Y. Lifshitz, S.T. Lee, *Adv. Mater.* **15**, 635 (2003).
13. C.R. Wang, K.B. Tang, Q. Yang, B. Hai, G.Z. Shen, C.H. An, W.C. Yu, Y.T. Qian, *Inorg. Chem. Commun.* **4**, 339 (2001).
14. C.R. Wang, K.B. Tang, Q. Yang, Y.T. Qian, *J. Electrochem. Soc.* **150**, G163 (2003).
15. M. Yazawa, M. Koguchi, A. Muto, M. Ozawa, K. Hiruma, *Appl. Phys. Lett.* **61**, 2051 (1992).
16. P.M. Aneesh, K.A. Vanaja, M.K. Jayara, *Nanophotonic Mater. IV Proc. of SPIE* **6639**, 66390J (2007).
17. S.W. Yan, H.J. Shun, L.C. Fuh, *J. Cryst. Growth* **310**, 2806 (2008).
18. C.H. Chen, S.J. Chang, S.P. Chang, M.J. Li, I.C. Chen, T.J. Hsuehand, C.L. Hsu, *Chem. Phys. Lett.* **476**, 69 (2009).
19. C.C. Lin, W.H. Lin, C.Y. Hsiao, K.M. Lin, Y.Y. Li, *J. Phys. D: Appl. Phys.* **41**, 045301 (2008).
20. J.P. Liu, C.X. Xu, G.P. Zhu, X. Li, Y.P. Cui, Y. Yang, X.W. Sun, *J. Phys. D: Appl. Phys.* **40**, 1906 (2007).
21. E. Oh, H.Y. Choi, S.H. Jung, S. Cho, J.C. Kim, K.H. Lee, S.W. Kang, J. Kim, J.Y. Yun, S.H. Jeong, *Sensor. Actuat. B Chem.* **141**, 239 (2009).
22. T. Zhang, Y. Zeng, H.T. Fan, L.J. Wang R. Wang, W.Y. Fu, H.B. Yang, *J. Phys. D: Appl. Phys.* **42**, 045103 (2009).
23. X. Ren, D. Chen, X. Meng, F. Tang, X. Hou, D. Han, L. Zhang, *J. Colloid Interface Sci.* **334**, 183 (2009).
24. A. Umar, A. Al-Hajry, Y.B. Hahn, D.H. Kim, *Electrochem. Acta* **54**, 5358 (2009).
25. F. Xu, Z.Y. Yuan, G.H. Du, T.Z. Ren, C. Bouvy, M. Halasa, B.L. Su, *Nanotechnol.* **17**, 588 (2006).
26. T.H. Mahato, G.K. Prasad, B. Singh, J. Acharya, A.R. Srivastava, R. Vijayaraghavan, *J. Hazard. Mater.* **165**, 928 (2009).
27. Y. Wang, X. Li, G. Lu, G. Chen, Y. Chen, *Mater. Lett.* **62**, 2359 (2008).
28. J.F. Hernandez-Sierra, F. Ruiz, D.C. Cruz Pena, F.M. Gutierrez, A.E. Martınez, A.J.P. Guillen, H.T. Perez, G.M. Castanon, *Nanomed. Nanotechnol. Biol. Med.* **4**, 237 (2008).
29. W. Lu, G. Liu, S. Gao, S. Xing, J. Wang, *Nanotechnol.* **19**, 445711 (2008).
30. Z. Yongnan, Y.U. Kwon, *Chem. Lett.* **33** No 12, 1578 (2004).
31. N. Jones, B. Ray, K.T. Ranjit, A.C. Manna, *FEMS Microbiology Lett.* **279**, 71 (2008).
32. L.K. Adams, D.Y. Lyon, P.J.J. Alvarez, *Water Res.* **40**, 3527 (2006).
33. O. Yamamoto, *Int. J. Inorganic Mater.* **3**, 643 (2011).
34. L. Zhang, Y. Jiang, Y. Ding, M. Povey, D. York, *J. Nanoparticle Res.* **9**, 479 (2007).
35. O. Seven, B. Dindar, S. Aydemir, D. Metin, M.A. Ozinel, S. Icli, *J. Photochem. Photobiology A: Chem.* **165**, 103 (2004).
36. G. Applerot, A. Lipovsky, R. Dror, N. Perkas, Y. Nitzan, R. Lubart, A. Gedanken, *Adv. Functional Mater.* **19** No 6, 842 (2009).
37. O. Yamamoto, J. Sawai, T. Sasamoto, *Mater. Transactions* **43**, 1069 (2002).
38. R. Brayner, R. Ferrari-Iliou, N. Brivois, S. Djediat, M.F. Benedetti, F. Fievet, *Nano Lett.* **6**, 866 (2006).
39. Y. Liu, L. He, A. Mustapha, H. Li, Z.Q. Hu, M. Lin, *J. Appl. Microbiol.* **107**, 1193 (2009).
40. K.H. Tam, A.B. Djurisic, C.M.N. Chan, Y.Y. Xi, C.W. Tse, Y.H. Leung, W.K. Chan, F.C.C. Leung, D.W.T. Au, *Thin Solid Films* **516**, 6167 (2008).
41. Z.B. Huang, X. Zheng, D.H. Yan, G.F. Yin, X.M. Liao, Y.Q. Kang, Y.D. Yao, D. Huang, B.Q. Hao, *Langmuir* **24**, 4140 (2008).
42. H. Akiyama, O. Yamasaki, H. Kanzaki, J. Tada, J. Arata, *J. Dermatological Sci.* **17**, 67 (1998).
43. T. Matsunaga, R. Tomoda, T. Nakajima, H. Wake, *FEMS Microbio. Lett.* **29**, 211 (1985).
44. P.C. Maness, S. Smolinski, D.M. Blake, Z. Huang, E.J. Wolfrum, W.A. Jacoby, *Appl. Environ. Microbio.* **65**, 4094 (1999).
45. S.V. Bhatt, M.P. Deshpande, S.H. Chaki, N.H. Patel, N. Pandya, B.H. Soni, *AIP Conf. Proc., Solid State Physics, Proceedings of the 55th DAE Solid State Physics Symposium 2010, December 26-30*, **1349**, 281 (2011).
46. G. Shuxia, D. Zuliang, D. Shuxi, *phys. status solidi b* **246**, 2329 (2009).
47. B. Yang, A. Kumar, N. Upia, P. Feng, R.S. Katiyar, *J. Raman Spectrosc.* **41**, 88 (2010).
48. K. Vanheusden, C.H. Seager, W.L. Warren, D.R. Tallant, J.A. Voigt, *Appl. Phys. Lett.* **68**, 403 (1996).
49. P.S. Xu, Y.M. Sun, C.S. Shi, F.Q. Xu, H.B. Pan, *Nucl. Instrum. Meth. A* **199**, 286 (2003).
50. E.G. Bylander, *J. Appl. Phys.* **49**, 1188 (1978).
51. M. Liu, A.H. Kitai, P. Mascher, *J. Lumin.* **54**, 35 (1992).
52. P.S. Xu, Y.M. Sun, C.S. Shi, F.Q. Xu, H.B. Pan, *Sci. China Ser. A* **44**, 1174 (2001).
53. S. Yuming, X. Pengshou, S. Chaoshu, X. Faqiang, P. Haibin, L. Erdong, *J. Electron Spectr. Related Phenomena* **114**, 1123 (2001).
54. A. Janotti, C.G.V. Walle, *J. Cryst. Growth* **287**, 58 (2006).
55. W.I. Park, Y.H. Jun, S.W. Jung, G.C. Yi, *Appl. Phys. Lett.* **82** No 6, 964 (2003).
56. S. Yun, J. Lee, J. Yang, S. Lim, *Physica B* **405**, 413 (2010).
57. N. Padmavathy, R. Vijayaraghavan, *Sci. Technol. Adv. Mater.* **9**, 035004 (2008).
58. J. Sawai, H. Kojima, H. Igarashi, A. Hashimoto, S. Shoji, A. Takehara, T Sawaki, T. Kokugan, M. Shimizu, *J. Chem. Eng. Japan* **30**, 1034 (1997).
59. J. Sawai, S. Shoji, H. Igarashi, A. Hashimoto, T. Kokugan, M. Shimizu, H. Kojima, *J. Ferment. Bioeng.* **86**, 521 (1998).
60. P.K. Stoimenov, R.L. Klinger, G.L. Marchin, K.J. Klabunde, *Langmuir* **18**, 6679 (2002).
61. R. Brayner, R. Ferrari-Iliou, N. Brivois, S. Djediat, M.F. Benedetti, F. Fiévet, *Nano Lett.* **6**, 866 (2006).
62. N. Jones, B. Ray, K.T. Ranjit, A.C. Manna, *FEMS Microbiol. Lett.* **279**, 71 (2008).
63. J. Sawai, *J. Microbiol. Methods* **54**, 177 (2003).